Updating the phase diagram of the archetypal frustrated magnet $Gd_3Ga_5O_{12}$

P. P. Deen
ESS, Tunavägen 24, 223 63 Lund, Sweden and Nanoscience Center, Niels Bohr Institute, University of Copenhagen, DK-2100 Copenhagen Ø, Denmark

O. Florea and E. Lhotel
Institut Néel, Centre National de la Recherche Scientifique and Université Joseph Fourier, BP 166, 38042 Grenoble Cedex 9, France

H. Jacobsen
Nanoscience Center, Niels Bohr Institute, University of Copenhagen, DK-2100 Copenhagen Ø, Denmark and ESS, Tunavägen 24, 223 63 Lund, Sweden

(Received 22 August 2014; revised manuscript received 11 November 2014; published 15 January 2015)

The applied magnetic field and temperature phase diagram of the archetypal frustrated magnet, $Gd_3Ga_5O_{12}$, has been reinvestigated using single-crystal magnetometry and polarized neutron diffraction. The updated phase diagram is substantially more complicated than previously reported and can be understood in terms of competing interactions with loops of spins, trimers, and decagons, in addition to competition and interplay between antiferromagnetic, incommensurate, and ferromagnetic order. Several additional distinct phase boundaries are presented. The phase diagram centers around a multiphase convergence to a single point at 0.9 T and ~ 0.35 K, below which, in temperature, a very narrow magnetically disordered region exists. These data illustrate the richness and diversity that arise from frustrated exchange on the three-dimensional hyperkagome lattice.

DOI: 10.1103/PhysRevB.91.014419 PACS number(s): 75.30.Kz, 75.30.Cr, 61.05.fm

I. INTRODUCTION

Frustration is ubiquitous in nature and drives the physical behavior in materials ranging from liquid crystals and polymers to compounds with localized magnetic moments [1–4]. The study of magnetic frustration, in particular, is proving very fruitful in the development of a more general understanding of frustrated phenomena. Magnetic frustration is governed by the connectivity of the many degenerate spin configurations in its ground-state manifold with geometric frustration borne out of the crystal structure topology. The multiplicity of ground states at the lowest temperatures, $T \rightarrow 0$ K, can lead to persistent dynamic magnetic spins [5], a most exotic state.

The rare-earth garnet $Gd_3Ga_5O_{12}$ (GGG) is unique since it offers a rare opportunity to study frustration on a double hyperkagome structure, a three-dimensional kagome lattice of interconnected triangles. GGG is regarded as the archetypal frustrated compound since, unlike its many counterparts, it does not revert to an ordered state via an "order by disorder" transition [6]. Indeed there is no sign of long-range order in GGG down to 0.025 K despite a Curie-Weiss temperature of $\theta_{CW} \sim -2$ K [7,8] indicating strongly frustrated antiferromagnetic (AF) correlations. In contrast, the rare-earth counterparts $Dy_3Ga_5O_{12}$ and $Ho_3Ga_5O_{12}$ order at relatively high temperatures, thereby highlighting the unique nature of the magnetic exchange interactions in GGG [7].

The leading magnetic interactions in GGG are the nearest-neighbor, $J_1 = -0.107$ K [8,9], and the dipole exchange interactions, $D = 0.0457$ K [10]. Adjacent triangle and sublattice exchange interactions, J_2 and J_3, respectively, are an order of magnitude smaller, $J_2 \sim -0.005$ and $J_3 \sim 0.010$ K [11]. In GGG the magnetic Gd^{3+} spins ($S = 7/2$) are considered as Heisenberg spins with single-ion anisotropy of less than 0.04 K. However, the non-negligible dipole exchange and the local crystal-field environment could lead to anisotropy [12]. The inherent spin Hamiltonian of the localized Gd^{3+} moment on the hyperkagome lattice gives rise to magnetic short-range order (SRO) below $T \sim 3$ K [8,10,13,14]. Below about 0.018 K, a spin-glass phase has been observed by ac susceptibility and specific heat at ambient fields [13] and verified by Petrenko *et al.* [14] using neutron scattering. Neutron scattering revealed sharper but not resolution limited magnetic diffraction peaks in addition to SRO for $T < 0.14$ K [14]. These correlations are understood to result from the long-range nature of the dipole exchange interactions perturbed by the very weak exchange interactions, J_2 and J_3 [11], and may give rise to a quantum protectorate of ten ion spin clusters [15].

The first (H,T) phase diagram of GGG indicated an AF dome with strong anisotropy such that applying the field along [1 0 0] creates an AF dome for $T < 0.4$ and $0.85 < \mu_0 H < 1.8$ T while applying the field along [1 1 1] results in an AF dome for $T < 0.3$ K and $0.9 < \mu_0 H < 1.4$ T [9]. The anisotropy of the phase diagram was further probed via magnetic susceptibility, specific heat, and single-crystal neutron scattering [16,17] and revealed that the phase diagram is much more complex than previously reported. The boundary between the disordered region above the spin-glass phase and the long-ranged AF dome showed considerable similarities with the melting curve of ^{4}He indicating unusual magnetic behavior in this region [18]. In contrast, muon spin relaxation and Mössbauer spectroscopy indicate a temperature spin relaxation indicative of slow spin fluctuations down to 0.025 K and up to 1.8 T [19–21]. The contradiction between a long-range ordered and dynamic magnetic state can be understood in terms of the time scales probed by the various techniques such that the system appears paramagnetic on the fast time scale of the muon but looks static within the energy resolution of the neutron. This has been observed in the frustrated magnet $Tb_2Ti_2O_7$, for which it was shown that there were many length and time scales to consider [22].

This study revisits the temperature- and field dependent behavior of GGG through macroscopic magnetic measurements of both powdered and single-crystal samples and a polarized neutron-scattering study of a powdered sample. In this study the field is applied along the [1 1 0] crystallographic direction to complement previous results. The phase diagram presents several additional phases for this direction of the applied magnetic field. These phases are also observed for the powder sample but are broadened, suggesting different characteristic field dependencies as a function of direction, as reported previously. Neutron powder diffraction correlates closely with the macroscopic measurements.

II. MAGNETIZATION MEASUREMENTS

A. Experimental details

Magnetization measurements were performed by the extraction method down to 0.08 K and up to 8 T, using a superconducting quantum interference device magnetometer equipped with a miniature dilution refrigerator, developed at the Institut Néel [23]. Two $Gd_3Ga_5O_{12}$ samples have been measured: (i) a 8.52-mg single crystal cut from a commercial ($10 \times 10 \times 0.4$ mm^3) substrate (Impex High Tech), measured along the [1 1 0] direction, and (ii) a 17.13-mg ^{160}Gd isotope powdered sample. Neutron-scattering experiments were performed on a powder sample of the same batch for a direct comparison. Magnetization measurements performed on the powder are in quantitative agreement with single-crystal measurements. However, the features are broadened, certainly due to the distribution of crystallites and the presence of a small anisotropy (∼0.04 K [12]). The results presented below are from the single-crystal sample. The field was applied in the plane of the substrate, so demagnetization corrections are negligible.

B. Phase diagram via magnetization measurements

Low-field magnetization measurements were performed by cooling down the sample from 4.2 to 0.08 K in an applied field of 10 mT. The susceptibility χ ($=M/H$ in low fields for which the magnetization is linear in field) as a function of temperature is shown in Fig. 1. The inset of Fig. 1 shows a monotonic decay of the inverse susceptibility with decreasing temperature. A linear behavior is observed down to 1.5 K and assumes a Curie-Weiss law between 1.5 and 4.2 K that provides a Curie constant of 8.13 emu/mol K, consistent with the Gd^{3+} spin moment, $S = 7/2$. The obtained Curie-Weiss temperature θ is -1.97 K in agreement with previous results [8,17]. Below 1 K, the plot deviates from the linear behavior, suggesting the development of correlations between the spins. In Fig. 2 isothermal magnetization measurements shows saturation around $M_{\rm sat} = 7\mu_B$/Gd. Above 2 K, no anomaly is seen in the magnetization curves.

A more complex behavior occurs below 1 K. To analyze the $M(H)$ curves as a function of temperature, dM/dH is plotted as a function of the applied field (see Fig. 3). The obtained features show much correspondence with the observations reported by Schiffer *et al.* [17] in heat-capacity and susceptibility measurements. Figure 3 shows the main features with a broad maximum for $H' \sim 1$ T that develops

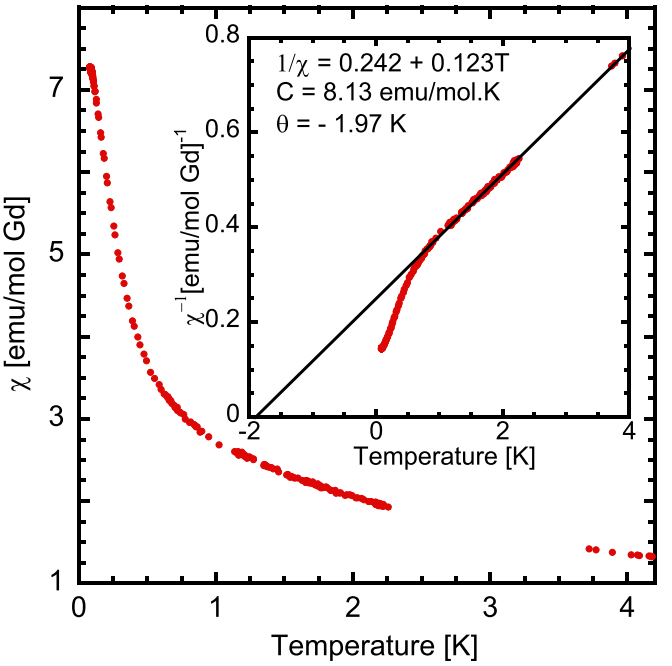

FIG. 1. (Color online) χ vs T at 0.01 T with $H \parallel$ to [1 1 0] for $0.08 < T < 4.2$ K. Inset: χ^{-1} vs T.

below 1 K. It has previously been assigned to the quenching of the AF short-range order (SRO). There is no significant change in the position or the width of this broad feature with decreasing temperature. Three well-defined peaks labeled H_1, H_2, and H_3 develop as the temperature is reduced below ∼ 0.34 K in addition to the broad feature centered around 1 T. The peaks at

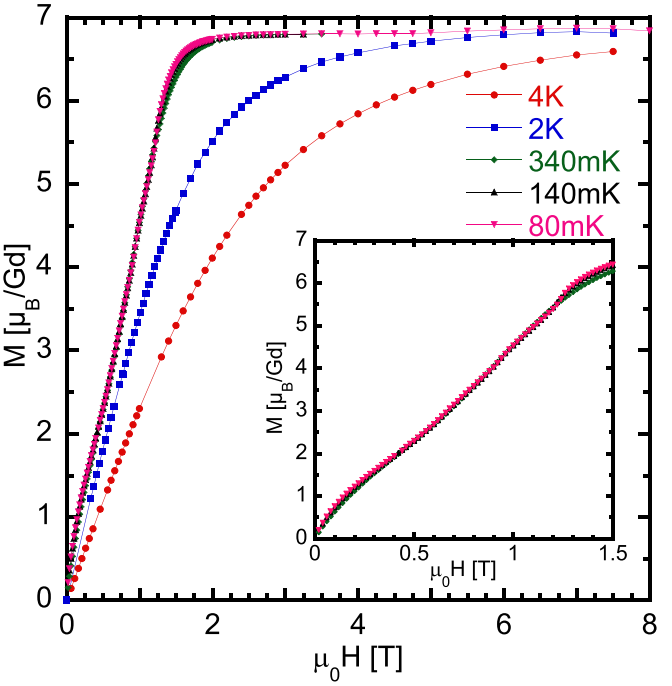

FIG. 2. (Color online) M vs $\mu_0 H$ for $0 < \mu_0 H < 7.5$ T with $H \parallel$ to [1 1 0] for several temperatures between 0.08 and 4.2 K. Inset: Zoom on the anomaly between 0 and 1.5 T at low temperature.

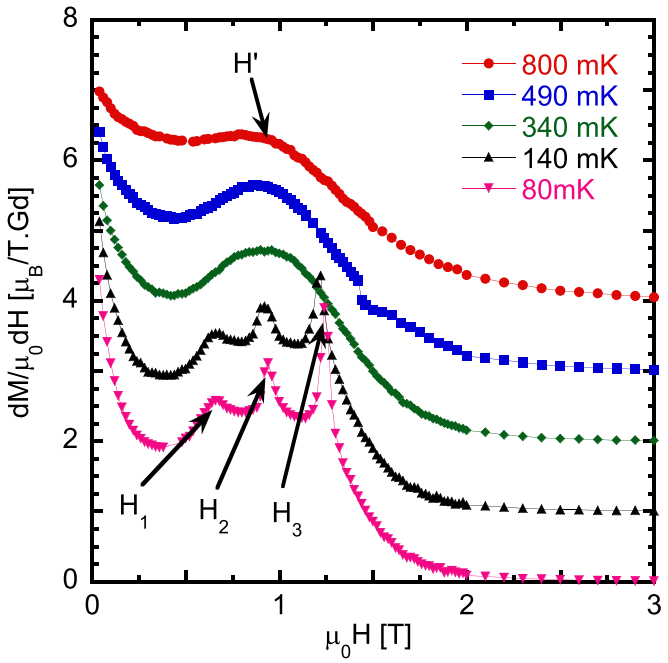

FIG. 3. (Color online) $dM/\mu_0 dH$ vs $\mu_0 H$ for a range of applied fields $0 < \mu_0 H < 8$ T with $H \parallel$ to [1 1 0]. The curves for different temperatures are separated by 1 μ_B for clarity. The intensity has been fitted with a Gaussian function for the broad feature and three Lorentzian functions for the three peaks.

the lowest field ($H_1 = \mu_0 H \sim 0.65$ T) and at the highest field ($H_3 = \mu_0 H \sim 1.25$ T) correspond to the boundaries of the previously observed field induced AF long-range order [17]. The temperature dependences of the peak positions are in good agreement with previous measurements, but their positions are slightly different, possibly the result of anisotropy. H_2 is a very clear and previously unreported peak at around $H_2 = \mu_0 H \sim 0.9$ T. A weak feature was also observed in this field range by Schiffer *et al.* [17], but it was much more rounded and of smaller amplitude. These three peaks, H_1, H_2, and H_3, grow on top of the broad SRO feature at H' but do not suppress it, confirming the coexistence between long-range and short-range ordering. It is worth noting that the newly reported H_2 peak is very sharp, similar to the H_1 and H_3 peaks which were identified as phase boundaries of the field induced ordered phase [9,17], thereby indicating that H_2 is the signature of a phase boundary. With increasing temperature the positions of the three peaks and of the broad feature converge toward a single point around $T^* \sim 0.35$ K at the magnetic field $\mu_0 H^* \sim 0.9$ T. To get a deeper understanding of this feature, we performed magnetization measurements as a function of temperature at a constant field.

At low fields, below 50 mT, the magnetization shows a freezing below 200 mK in the zero-field cooled–field cooled (ZFC-FC) measurements, as previously reported [17]. This freezing was also observed in our ac susceptibility measurements. Above 50 mK, this ZFC-FC irreversibility disappears. In the following we focus on larger applied fields to further explore the phase diagram in comparison with our M versus H measurements. Figure 4 shows ZFC-FC temperature-dependent magnetization measurements for a range of applied magnetic fields: Fig. 4(a), $0.4 \leqslant \mu_0 H \leqslant 0.7$ T; Fig. 4(b), $0.8 \leqslant \mu_0 H \leqslant 0.9$ T; and Fig. 4 (c), $1.0 \leqslant \mu_0 H \leqslant 1.3$ T. The magnetic field dependence can be subdivided into five distinct behaviors. First, $\mu_0 H < 0.4$ T. ZFC and FC magnetizations overlay and decay monotonically with increasing temperature. No magnetic ordering is observed in this field range. Second, for $0.5 < \mu_0 H < 0.7$ T, two distinct features are observed: a broad maximum around $T_1 = 0.6$ K and a change in slope around $T_2 = 0.2$ K. T_1 shifts to lower temperatures when the magnetic field is increased. Third, for $0.8 < \mu_0 H < 0.9$ T, the two features overlap so that no clear maximum emerges. A splitting in the ZFC-FC measurements occurs at $\mu_0 H^* = 0.9$ T below $T \sim 0.2$ K. This ZFC-FC hysteresis is quantitatively reproducible and is present in a very narrow field region around 0.9 T. The ZFC-FC splitting concerns 7% of the magnetization. Fourth, for $0.9 < \mu_0 H < 1.2$ T, the curves recovers the shape of the $0.5 < \mu_0 H < 0.7$-T region. Fifth, for $\mu_0 H > 1.3$ T, the magnetization decreases continuously with increasing temperature.

An updated phase diagram can be constructed from these measurements and is shown in Fig. 5 and Table I. High temperatures, T_1 (orange circles) above H' (violet squares), can be associated with the SRO features previously observed in specific-heat and susceptibility measurements by Schiffer *et al.* [17]. However, the low-temperature change in slope around T_2 (red squares) indicates an evolution of the SRO state,

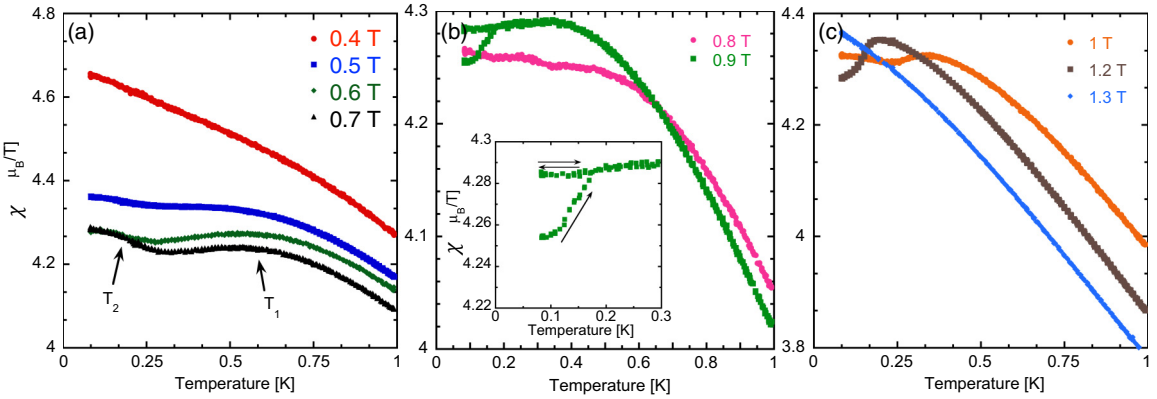

FIG. 4. (Color online) χ vs T measured with a ZFC-FC procedure for a range of applied fields $0.4 < \mu_0 H < 1.3$ T along the [1 1 0] direction.

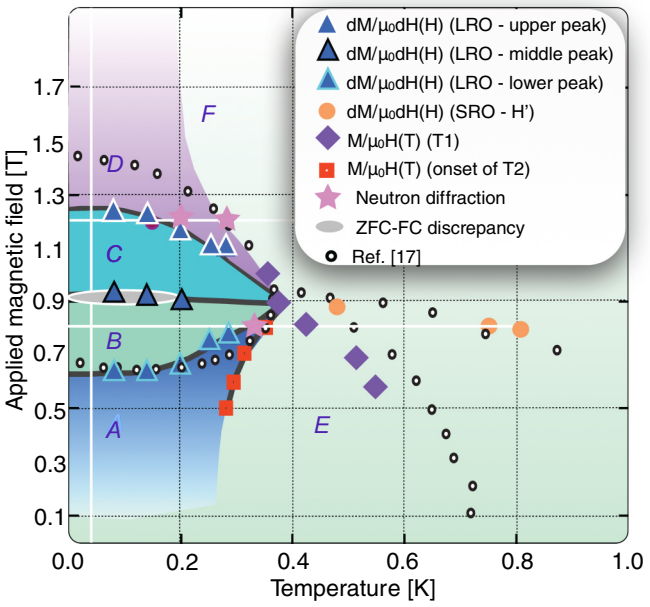

FIG. 5. (Color online) The updated phase diagram of $Gd_3Ga_5O_{12}$ determined from macroscopic magnetization measurements and neutron powder diffraction. The continuous white lines show regions measured in this study using neutron diffraction.

which thus can be separated into two regions (A-E) separated at the onset of T_2. H_1 and H_3 (blue triangles) match the AF field induced region previously observed. The new observed peak in M versus $\mu_0 H$ measurements at $H_2 = \mu_0 H = 0.9$ T (violet triangles) divides the AF field induced region into two phases (B-C). At this (B-C) phase boundary, $\mu_0 H \sim 0.9$ T, $T < 0.2$ K, a small region is reported in which a ZFC-FC discrepancy is observed. Interestingly this phase boundary corresponds to the development of field induced phases and the collapse of SRO more explicitly probed using neutron scattering. As such it makes $\mu_0 H = 0.9$ T, $T \sim 0.35$ K a specific point in the phase diagram of GGG. In the following section these results are compared with the coexistence of short-range, incommensurate, and AF phases as observed by Petrenko *et al.* [14] and extended in this work using neutron diffraction.

III. NEUTRON DIFFRACTION

This study focuses on the regions of the phase diagram encompassing $0.175 < T < 3$ K ($\mu_0 H = 0$ T) and $0.06 < T < 3$ K ($0 < \mu_0 H < 2$ T). The unusual scattering observed for $T < 0.14$ K in zero field with longer-ranged order superposed on short-range correlations is not considered. Neutron scattering corroborates the complicated phase diagram shown in Fig. 5 with strong consistency between magnetization and neutron-diffraction measurements.

Petrenko *et al.* [16] concluded that competing magnetic interactions result in competition between various ground states and prevent GGG from ordering in zero magnetic field, while applying a small magnetic field crystalizes the magnetic state into ordered components with a range of ferromagnetic (FM), AF, and incommensurate (IC) propagation vectors.

The present work provides a greater insight into the interplay between different magnetic orders. Particular emphasis is placed on the perturbation of the short-range order with respect to the other magnetically ordered states. Short-range magnetic order pervades the (H,T) phase in which uniquely long-range magnetic correlations have previously been assigned. The interplay between short-range, FM, AF, and IC orders is correlated with the phase diagram outlined in Fig. 5 and with the main results condensed in Table I. These data sets highlight why a refinement of the magnetic structure with a single wave vector has eluded previous studies.

TABLE I. Outline of the phase diagram presented in Fig. 5. SRO = short-range order, M = magnetization, NS = neutron scattering.

Phase T (K) $\mu_0 H$ (T)	M signature	NS signature
A: ($T < 0.25, \mu_0 H < 0.65$])	Slope change (T_2)	(1) Broad feature at 0.8 Å^{-1} (2) Broad feature at 0.8 Å^{-1} (3) Development of IC and AF peaks
E: ([0.25; 1], $\mu_0 H < 0.9$)	Broad maximum (T_1)	(1) Loss of AF (1.14 Å^{-1}) and IC (1.08 Å^{-1}) (2) Decrease of SRO
B: ($T < 0.35$, [0.65; 0.9])	Three peaks in $\frac{dM}{\mu_0 dH}$	(1) IC peak → [2 1 0] (2) Loss of IC peaks [1 1 0] → [$\frac{3}{2}$ 1 $\frac{1}{2}$]
C: ($T < 0.35$, [0.65; 0.9])	Irreversible ZFC-FC	(1) IC peak between [2 0 0] and [2 1 0] fixed in Q (2) Scattering at $Q = 1.69$ Å^{-1} (3) SRO more correlated
D: ($T < 0.2, \mu_0 H > 1.2$)	No signature	(1) Development of scattering at 0.8 Å^{-1} (2) Loss of first SRO peak (3) Appearance of IC peak at $Q = 0.80(2)$ Å^{-1} (4) Loss of Bragg peak at 1.69 Å^{-1}
F: ([0.2; 1], $\mu_0 H > 0.9$)	No signature	(1) Loss of [2 1 0] scattering (2) Weak variation of [2 0 0] Bragg-peak intensity

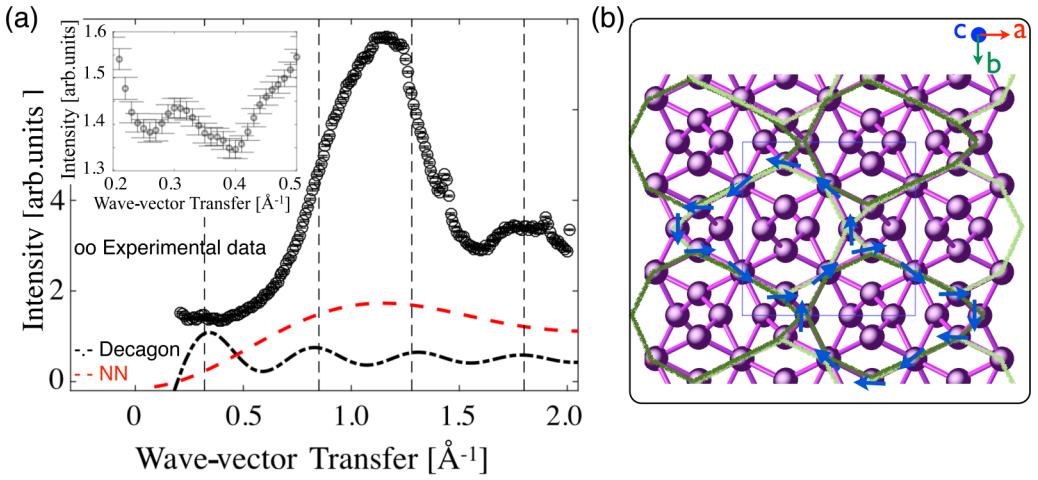

FIG. 6. (Color online) (a) Neutron diffraction of $Gd_3Ga_5O_{12}$ at 0.25 K, 0 T with a nearest-neighbor (NN) spin model (red line–) and exchange between ten ion spin clusters (black -.-) for comparison. Inset: Zoom of the magnetic scattering around $Q = 0.3$ Å^{-1}. (b) Snapshot of ions involved in the ten ion spin cluster for the [1 0 0]/[0 1 0] crystallographic direction. The blue rectangle is the structural unit cell. The light green and light blue loops show two domains. The arrows denote the relative spin directions of the ions.

A. Experimental details

Neutron-scattering experiments were performed on the D7 diffuse scattering spectrometer and the cold chopper spectrometer IN5 at the Institut Laue Langevin, Grenoble. The sample has previously been used in the work of Petrenko *et al.* [14] and Deen *et al.* [24] containing 99.98% of the nonabsorbing isotope ^{160}Gd. The sample was covered with isopropanol (or 2-propanol) 99% deuterium that freezes the crystallites into place without any substantial contribution to the scattering.

The zero-field data, measured on IN5, show the scattering within the elastic resolution of the instrument, 80 μeV full width at half maximum. The energy resolution is determined using a standard incoherent scatterer (see Sec. III C 1). The IN5 data set could not be integrated in energy due to spurious scattering in parts of the inelastic spectrum.

The field-dependent data have been measured using D7 with $E_I = 3.55$ meV. The wide angular range available on D7 enables simultaneous determination of short- and long-ranged scattering and elucidates their interplay. Field-dependent measurements up to 2.5 T were performed at 0.05 K with a temperature dependence measured, up to 0.8 K, at 0.8 and 1.2 T, as depicted by the white continuous lines in Fig. 5. Uniaxial polarization analysis performed under applied field on D7 provides two scattering cross sections, spin-flip and non-spin-flip scattering. The spin-flip scattering is entirely magnetic in origin since the spin-incoherent cross section for GGG is negligible. The non-spin-flip scattering contains nuclear and magnetic components. A separation of the spin-flip from the non-spin-flip contributions allows the nuclear scattering to be isolated while the spin-flip contributions provide the magnetic cross sections [25]. The data have been corrected for detector and polarization analyzer efficiencies using standard samples of vanadium and amorphous silica, respectively [25]. All data are corrected for background contributions by subtracting the scattering from an empty sample can under equivalent conditions. The D7 data set is integrated in energy. Nevertheless the data sets from D7 and IN5 can be compared since previous work shows that the majority of the scattering is elastic (82%) and the features of interest for this study lie solely in the elastic line [24,26]. This is discussed further in the Appendix.

B. Ambient field behavior

Region A, depicted in the phase diagram of Fig. 5, has generally been considered to consist of short-range magnetic correlations. Petrenko and Paul [27] determined, using Monte Carlo methods, nearest-neighbor interactions, $J_1 = 0.107$ K, as the dominant magnetic exchange term. Upon closer inspection of the scattering profiles [see Fig. 6(a)], it can be seen that a model with only nearest-neighbor exchange cannot give rise to the scattering profile observed. Instead, it is proposed that a self-organized superlattice unit, a ten ion spin cluster, is required to account for some of the features [see Fig. 6(b)]. The arguments behind such a model are presented in the next few paragraphs.

Short-range magnetic correlations in a powder sample scatter according to the expression

$$\left(\frac{d\sigma}{d\Omega}\right)_{\text{Mag}} \sim \sum_n \frac{\langle \mathbf{S_0} \cdot \mathbf{S_n} \rangle}{S(S+1)} N_n \frac{\sin(QR_n)}{QR_n} F(Q), \qquad (1)$$

where S_0 and S_n are the spin magnitudes of the central atom and the nth shell atom; R_n and N_n are the radii and coordination numbers of the nth nearest-neighbor shell, respectively [28]; and $F(Q)$ is the magnetic form factor [29,30]. Figure 6(a) shows the expected magnetic scattering profile for short-range order, using Eq. (1), in comparison to the magnetic scattering profile measured at $T = 0.25$ K (0 T). Interestingly, the short-range order profile does not reproduce all the features expected, in particular, the broad feature centered on $Q = 1.8$ Å^{-1}. In order to reproduce scattering at $Q = 1.8$ Å magnetic exchange between ten ion spin clusters is considered.

In recent years there has been much excitement surrounding emergent behavior in geometrically complex materials. The kagome lattice has provided such an emergent structure in

the form of correlated hexagon loops of spins [31]. It has been suggested that the first- and second-order zero-energy modes on the hyperkagome structure are dynamic loops of spins that include triangular loops of spins, trimers, and ten ion spin clusters, decagons [32–34]. The interpretation from recent optical hole-burning experiments supports the existence of ten ion spin clusters in the low-temperature spin-glass phase of GGG [15]. Figure 6(b) shows a snapshot, in time, of possible spin directions involved in such a ten ion spin cluster for the [1 0 0]/[0 1 0] crystallographic directions. The loops are decoupled from their environments and suggested to be quantum protectorates [35,36]. The magnetic exchange for trimers can be modeled using Eq. (1) with only nearest-neighbor exchange and the requirement that Heisenberg spins on a triangular lattice $\sum_{\text{triangle}} S = 0$, resulting in nearest-neighbor spins 120° relative to each other. The magnetic neutron-scattering profile for a trimer [see Fig. 6(a)] shows a maximum in scattering intensity at the same Q position as nearest-neighbor magnetic correlations, $Q \sim 1.1$ Å^{-1}. The spins on a decagon loop also obey the Heisenberg nearest-neighbor spin requirement yet the spins are correlated throughout the ten ion spin cluster. The exchange between ten spin ion clusters can be described using Eq. (1) to consider short-range interactions between adjacent clusters. The coordination number of a ten ion spin cluster is 14 with an average unit-cell size of 13.12 Å. The magnetic scattering from ten ion spin clusters [see Fig. 6(b)] provides many extra features in common with the powder-diffraction data of GGG at 0.25 K and 0 T.

The models show that using a combination of nearest neighbors interactions and exchange between ten spin ion clusters can explain some experimental features. First, around $Q \sim 0.3$Å^{-1} there is a weak feature consistent with the position of the first peak of the ten ion spin cluster [see inset of Fig. 6(a)]. Second, the main peak of the nearest-neighbor model is found at the same position as the main peak in the data, however this peak is strongly asymmetric and this can be ascribed to scattering from ten ion spin clusters which provides two features either side of the main peak position [see dashed lines in Fig. 6(a)]. Third, a strong scattering feature at 1.8 Å^{-1} in the ten ion spin cluster model is consistent with the data. Interestingly, the magnetic correlation length $\xi = 2\pi/\Delta Q$ of the SRO peak at 1.8 Å^{-1} corresponds to an average unit-cell size of the ten ion spin clusters, $\xi = 13.8 \pm 2$ Å. A combination of these two models captures the position of the scattering if not perfectly the respective weights of the scattering. Nevertheless it provides a strong indication of unusual correlations such as the coexistence of nearest-neighbor exchange with a ten ion spin cluster. This data set therefore captures the first two soft modes of spins on hyperkagome structure, dynamic trimer, and decagon spin loops as a feature of region A.

C. Magnetic behavior under applied magnetic fields

1. Field dependence ($T = 0.05$ K)

An overview of the field dependence of the magnetic scattering is shown in Fig. 7 and reveals great complexity. Peaks corresponding to AF peak positions are marked with continuous blue lines while FM peak positions are marked by dashed black lines. The phase boundaries reported in Fig. 5 are reproduced in Fig. 7. Variations in the magnetic scattering profiles can be accurately mapped onto the phase diagram as described in Table I. A closer look at the individual scattering profiles for each applied magnetic field provides more detailed information.

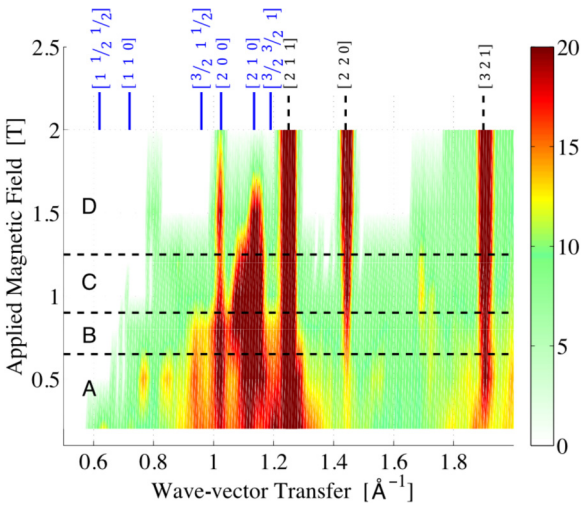

FIG. 7. (Color online) Overview of the field dependence of the magnetic neutron scattering at 0.05 K. Peaks corresponding to AF peak positions are marked with full vertical blue lines while FM peak positions are marked by dashed vertical black lines. The phase boundaries found in Fig. 5 are presented by dashed horizontal lines.

Figure 8(a) shows magnetic scattering profiles in region A → H for 0, 0.2, and 0.5 T ($T < 0.25$ K). The scattering profile at 0.25 K, 0 T is the elastic scattering within the energy resolution, 80 μeV of IN5; further information is provided in the Appendix. Upon the application of only 0.2 T the short-ranged ordered peaks are drastically reduced. This is particularly true for the first SRO peak at $Q \sim 1.1$ Å^{-1}. Interestingly, the second SRO peak, assigned to scattering from a decagon loop in the previous section, is more robust and remains unaffected up to 0.5 T. This would indicate

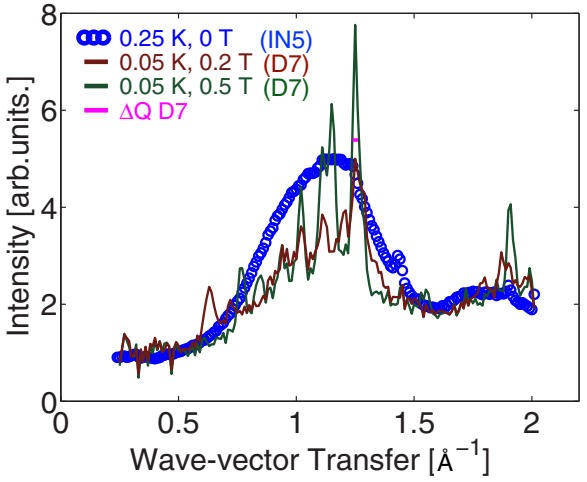

FIG. 8. (Color online) (a) Field dependence of magnetic neutron diffraction at 0.25 K and 0 T, 0.05 K and 0.2 T, and 0.05 K and 0.5 T.

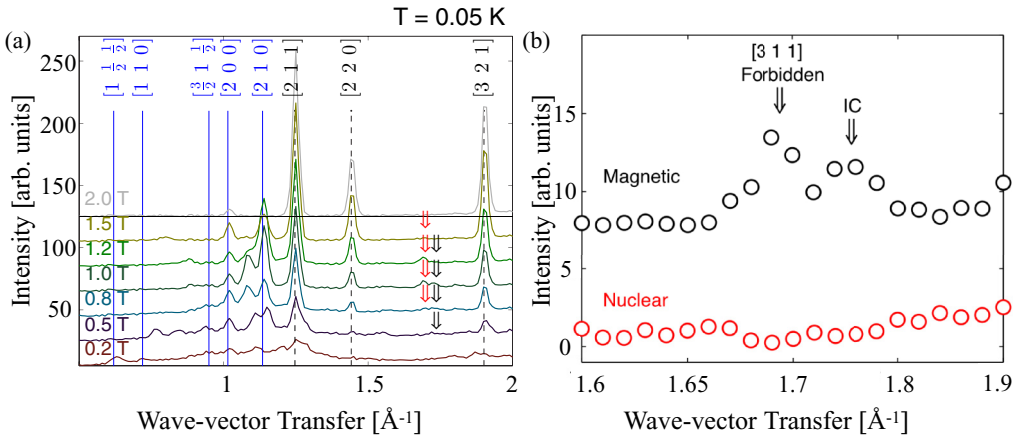

FIG. 9. (Color online) (a) Field dependence of the magnetic scattering at 0.05 K. The continuous blue vertical lines correspond to order that is commensurate with the crystal structure and could represent AF order. Dashed black vertical lines are nuclear or FM positions. The vertical arrows denote scattering at the forbidden nuclear scattering position [3 1 1] and an IC position. The data are offset for clarity. (b) Scattering profiles of the magnetic and nuclear contributions at 0.05 K and 1 T zoomed in on the region of the scattering at 1.69 and 1.72 Å^{-1}. The nuclear profile shows no equivalent scattering.

that decagons are more resilient to perturbation than the trimer counterparts upon the application of a magnetic field. Longer-ranged correlations are developed by 0.2 T and are resolution limited at 0.5 T (see Fig. 8).

Figure 9(a) shows the complete field dependence of the magnetic diffraction patterns at base temperature, 0.05 K. FM correlations are not considered in this work since it is impossible to disentangle the effect of local magnetic exchange interactions and the increase in scattering at the nuclear Bragg-peak positions due to the application of a magnetic field on a powder. The data are offset for clarity. The continuous vertical lines correspond to positions in reciprocal space where AF order is expected while dashed vertical lines are positions corresponding to nuclear or FM order. In region A, $0 < \mu_0 H < 0.65$ T, the IC features observed between the [1 1 0] and [$\frac{3}{2}$ 1 $\frac{1}{2}$] Bragg-peak positions and for $Q < 1.2$ Å^{-1} are very fluid with respect to their absolute position in reciprocal space. This is particularly true for the broad features around 0.6–0.8 Å^{-1} at 0.2 T that have shifted to between 0.7 and 0.9 Å^{-1} by 0.5 T and are not observed beyond. The boundary between phases A and B fixes the Bragg positions of various AF and IC Bragg peaks. An example is the [2 1 0] Bragg-peak position which appears to move from an IC position in phase A to the [2 1 0] Bragg-peak position in phase B. Additionally, the IC scattering between [2 0 0] and [2 1 0] is also fixed into position as the A-B phase boundary in crossed. Upon the establishment of phase C, $0.9 < \mu_0 H < 1.2$ T, magnetic scattering for $Q < 0.8$ Å^{-1} is diminished and magnetic scattering appears at $Q = 1.69(2)\text{Å}^{-1}$. Interestingly this scattering corresponds to the [3 1 1] Bragg-peak position, forbidden in neutron scattering for this crystallographic symmetry. This scattering could then be the result of either a magnetic phase change or a signature of magnetoelastic coupling (MEC). MEC can be a very weak effect, possibly the result of a slight rotation of oxygen around the dodecahedral Gd^{3+} site. However, MEC should also give rise to scattering in the nuclear channel, however neutron scattering might not be sufficiently sensitive to reveal the nuclear scattering part. Indeed there is no nuclear scattering peak at the [3 1 1] Bragg-peak position when comparing the magnetic scattering cross section to the nuclear scattering cross section [see Fig. 9(b)], so the origin of this scattering remains unclear.

Region D is consistent with the complete loss of the first SRO peak, the appearance of an IC Bragg peak at $Q = 0.80(2)\text{Å}^{-1}$, and the loss of the Bragg peak at $Q = 1.69(2)$ Å^{-1}. Although the first SRO peak has disappeared in this region, the second SRO peak, at $Q = 1.8$ Å^{-1}, remains strong up to and beyond 2.0 T. Above 1.5 T, all AF peaks are suppressed except the AF peak at 1.01 Å ([2 0 0]), which persists.

An overview of the field-dependent behavior of the integrated intensities of some of the magnetic scattering is given in Fig. 10. It is particularly interesting to note the interplay between the various magnetic contributions such that the AF scattering at $Q = 1.14$ Å^{-1}, ([2 1 0]), is most intense when

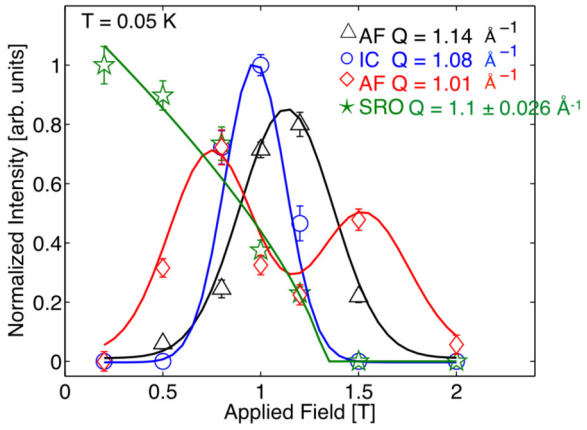

FIG. 10. (Color online) Field dependent integrated intensities of AF, IC, and short-range order. The data are normalized for ease of viewing and the lines through the data are to guide the eye.

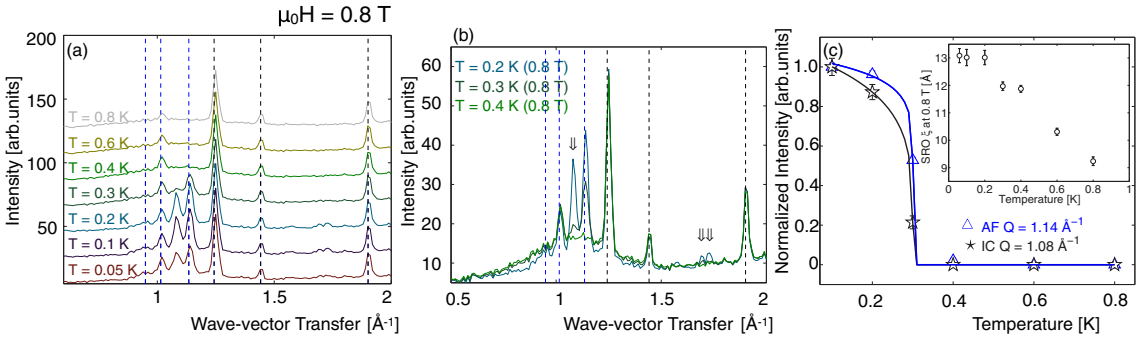

FIG. 11. (Color online) (a) Temperature dependence of the magnetic scattering at 0.8 T. The data are offset for clarity. The blue dashed vertical lines correspond to AF order. Dashed vertical lines are nuclear or F positions. (b) Focus on the region $0.2 < T < 0.4$ K (0.8 T). The black arrows emphasize the greatest variations in this temperature range. (c) Temperature dependence of the integrated intensities of the AF ($Q = 1.14$ Å^{-1}) and IC ($Q = 1.08$ Å^{-1}) clearly showing the phase transition A → E defined in Fig. 5. Inset: Temperature dependence of ξ for the first SRO peak.

the AF scattering at $Q = 1.01$ Å^{-1} ([2 0 0]) is much reduced only for the $Q = 1.14$ Å^{-1} peak to restrengthen when the $Q = 1.01$ Å^{-1} peak diminishes, region D. In addition, the field dependence of the IC peak at 1.08 Å^{-1} follows the integrated intensities of the AF peak at $Q = 1.14$ Å^{-1}.

2. *Temperature dependence at 0.8 T (T = 0.05 K)*

The magnetization data imply a convergence of phases to a unique point around 0.9 T and 0.35 K. Temperature-dependent powder diffraction has been measured at 0.8 T to determine the unique nature of this region [see Figs. 11(a) and 11(b)], with particular emphasis on the region $0.2 < T < 0.4$ K. These data show a very distinct transition at 0.3 K with both AF and IC orders disappearing beyond 0.3 K [see Fig. 11(c)]. The line separating regions A → E is observed in the neutron-scattering profiles. The magnetic scattering correlation of the first SRO peak broadens beyond 0.2 K from 13.1(3) Å at the lowest temperatures to 9.2(2) Å at 0.8 K [see inset of Fig. 11(c)]. It is difficult to extract ξ for the second short-range ordered peak due to its weaker nature and limited Q range. The magnetic scattering at the IC position, $Q = 1.73$ Å^{-1}, and the forbidden nuclear Bragg-peak position $Q = 1.69$ Å^{-1} disappear between 0.2 and 0.3 K [see the black arrows on Fig. 11(b)]. These data do indeed indicate that there is a convergence of phases around 0.9 T and 0.35 K as indicated in Fig. 5, however more detailed studies are needed to elucidate the precise details of this region.

3. *Temperature dependence at 1.2 T*

The neutron-scattering data of the 1.2-T temperature dependence (Fig. 12) traverses regions C → D → F. The IC peak at 1.08 Å disappears between $0.2 < T < 0.3$ K [black arrow in Fig. 12(b)], region C → D. The peak at the position of the forbidden nuclear Bragg peak, $Q = 1.69$ Å^{-1}, in addition to the AF Bragg peak at $Q = 1.14$ Å^{-1}, disappear between $0.3 < T < 0.4$ K, region D → F. Interestingly the peak at $Q = 1.01$ Å^{-1}, a peak that can be attributed to AF order, is only slightly perturbed in the $0.3 < T < 0.4$-K region. Figure 12(c) shows the variation in scattering profiles across the F → E transition. A slight variation in intensity is observed but no clear transition can be observed via neutron diffraction. Single-crystal measurements are required to elucidate the details of the variation in scattering to determine whether the regions E and F are distinct phases.

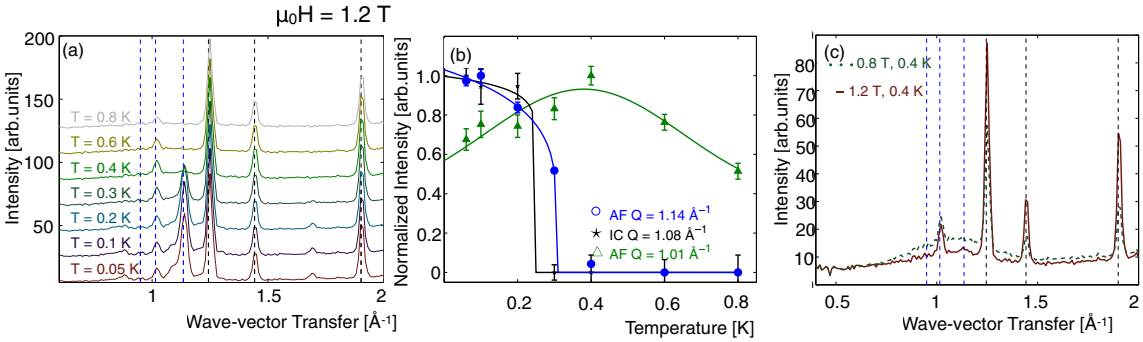

FIG. 12. (Color online) (a) Temperature dependence of $Gd_3Ga_5O_{12}$ at 1.2 T. The data are offset for clarity. The blue dashed vertical lines correspond to AF order. Black dashed vertical lines are nuclear or FM positions. (b) Integrated intensity of AF and IC Bragg peaks. Lines are a guide to the eye. The arrows show regions' greatest variation in this temperature range. (c) Neutron scattering profiles across the phase boundary E → F. No clear transition is apparent.

IV. CONCLUSION

An investigation of the applied magnetic field and temperature-dependent behavior of the archetypal magnetically frustrated compound $Gd_3Ga_5O_{12}$ is presented. Single-crystal and powder magnetic susceptibility in conjunction with polarized neutron diffraction reveal a unified picture of the phase diagram with close correlation between magnetic susceptibility measurements with the field applied along the [1 1 0] crystalline direction and neutron-scattering profiles of a powdered sample.

Several extra phase boundaries are required to correctly describe the (H,T) phase diagram of GGG with $H \parallel$ [1 1 0]. There is strong evidence that trimerized and decagon loops of spins coexist at low temperatures and low magnetic fields. These emergent loops of spins are strongly affected by the long-range ordered components yet coexist with incommensurate and AF order up to 1.3 T for spin trimers and beyond 2.0 T for decagon spin structures. Magnetization measurements allude to a multiphase convergence around 0.9 T and 0.35 K. Interestingly, there is a strong ZFC-FC discrepancy at 0.9 T and $T < 0.2$ K that is very well defined in applied field, indicative of a further glassy phase. The close link between susceptibility and neutron powder scattering thus indicates that the behaviors observed exist throughout the crystal, originate from the spin Hamiltonian on the hyperkagome lattice, and are an intrinsic feature of frustration on hyperkagome structures.

ACKNOWLEDGMENTS

The project was partly funded by the Danish Re-449 Search Council for Nature and Universe through Danscatt. P.D. would like to thank the sample environment group at the Institut Laue Langevin for their support and H. Mutka and O.A Petrenko for stimulating discussions. We would like to thank C. Paulsen for the use of his magnetometers and J. Debray for the orientation of the single crystal. O.F. acknowledges a grant from the Laboratoire d'Excellence Laboratoire d'Alliances Nanosciences-Energies du Futur in Grenoble.

[1] B. Lotz, Macromolecules **45**, 2175 (1912).
[2] T. Araki, M. Buscaglia, T. Bellini, and H. Tanaka, Nature Materials **10**, 303 (2011).
[3] L. Balents, Nature (London) **464**, 199 (2010).
[4] J. S. Gardner, M. J. P. Gingras, and J. E. Greedan, Rev. Mod. Phys. **82**, 53 (2010).
[5] P. Mendels, C. Lacroix, and F. Mila, *Introduction to Frustrated Magnetism*, Springer Series in Solid State Sciences Vol. 164 (Springer, New York, 2011).
[6] J. Villain, R. Bidaux, J. P. Carton, and R. J. Conte, J. Phys. (Paris) **41**, 1263 (1980).
[7] D. G. Onn, H. Meyer, and J. P. Remeika, Phys. Rev. **156**, 663 (1966).
[8] W. I. Kinney and W. P. Wolf, J. Appl. Phys. **50**, 2115 (1979).
[9] S. Hov, H. Bratsberg, and A. T. Skjeltorp, J. Magn. and Magn. Mater. **15–18**, 455 (1980).
[10] O. A. Petrenko and D. McK. Paul, Phys. Rev. B **63**, 024409 (2000).
[11] T. Yavors'kii, M. Enjalran, and M. J. P. Gingras, Phys. Rev. Lett. **97**, 267203 (2006).
[12] J. Overmeyer, *Paramagnetic Resonance* (Academic, New York, 1963), Chap. 15.
[13] P. Schiffer, A. P. Ramirez, D. A. Huse, P. L. Gammel, U. Yaron, D. J. Bishop, and A. J. Valentino, Phys. Rev. Lett. **74**, 2379 (1995).
[14] O. A. Petrenko, C. Ritter, M. Yethiraj, and D. McK. Paul, Phys. Rev. Lett. **80**, 4570 (1998).
[15] S. Ghosh, T. F. Rosenbaum, and G. Aeppli, Phys. Rev. Lett. **101**, 157205 (2008).
[16] O. A. Petrenko, G. Balakrishnan, D. McK. Paul, M. Yethiraj, G. J. McIntyre, and A. S. Wills, J. Phys.: Conference Series **145**, 012026 (2009).
[17] P. Schiffer, A. P. Ramirez, D. A. Huse, and A. J. Valentino, Phys. Rev. Lett. **73**, 2500 (1994).
[18] Y. K. Tsui, C. A. Burns, J. Snyder, and P. Schiffer, Phys. Rev. Lett. **82**, 3532 (1999).
[19] S. R. Dunsiger, J. S. Gardner, J. A. Chakhalian, A. L. Cornelius, M. Jaime, R. F. Kiefl, R. Movshovich, W. A. MacFarlane, R. I. Miller, J. E. Sonier, and B. D. Gaulin, Phys. Rev. Lett. **85**, 3504 (2000).
[20] I. M. Marshall, S. J. Blundell, F. L. Pratt, A. Husmann, C. A. Steer, A. I. Coldea, W. Hayes, and R. C. C. Ward, J. Phys.: Condens. Matter **14**, L157 (2002).
[21] P. Bonville, J. A. Hodges, J. P. Sanchez, and P. Vulliet, Phys. Rev. Lett. **92**, 167202 (2004).
[22] P. J. Baker, M. J. Matthews, S. R. Giblin, P. Schiffer, C. Baines, and D. Prabhakaran, Phys. Rev. B **86**, 094424 (2012).
[23] C. Paulsen, *Introduction to Physical Techniques in Molecular Magnetism: Structural and Macroscopic Techniques—Yesa 1999* (University of Zaragoza, Zaragoza, 2001).
[24] P. P. Deen, O. A. Petrenko, G. Balakrishnan, B. D. Rainford, C. Ritter, L. Capogna, H. Mutka, and T. Fennell, Phys. Rev. B **82**, 174408 (2010).
[25] J. R. Stewart, P. P. Deen, K. H. Andersen, H. Schober, J.-F. Barthélémy, J. M. Hillier, A. P. Murani, T. Hayes, and B. Lindenau, Journal of Applied Crystallography **42**, 69 (2009).
[26] P. P. Deen, H. Mutka, O. A. Petrenko, and N. d'Ambrumenil (unpublished).
[27] O. A. Petrenko and D. McK. Paul, AIP Conf. Proc. **479**, 90 (1999).
[28] B. D. Rainford, J. Physique **43**, C7 (1982).
[29] J. Brown, International Tables for Crystallography **C**, 454 (2006).
[30] G. L. Squires, *Introduction to the Theory of Thermal Neutron Scattering* (Dover, New York, 1978).
[31] S. H. Lee, C. Broholm, W. Ratcliff, G. Gasparovic, Q. Huang, T. H. Kim, and S. W. Cheong, Nature (London) **418**, 856 (2002).
[32] E. J. Bergholtz. A. M. Läuchli, and R. Moessner, Phys. Rev. Lett. **105**, 237202 (2010).
[33] M. E. Zhitomirsky, Phys. Rev. B **78**, 094423 (2008).
[34] J. Robert, B. Canals, V. Simonet, and R. Ballou, Phys. Rev. Lett **101**, 117207 (2008).
[35] R. D. Laughlin and D. Pines, Proc. Natl. Acad. Sci. USA **97**, 28 (2000).
[36] A. L. Kuzemsky, International Journal of Modern Physics B **24**, 835 (2011).